ACS APPLIED NANO MATERIALS

www.acsanm.org Article

Fabrication of SERS Substrates Using Silver-Coated Gold Nanostars for Chemical Sensing: A Multiobjective Bayesian Optimization Approach

Andrea N. Giordano,* Samuel Franqui-Rios, Steven M. Quarin, Der Vang, Drake R. Austin, Abigail G. Doyle, Luke A. Baldwin, Pietro Strobbia, and Rahul Rao*

Cite This: https://doi.org/10.1021/acsanm.5c01462 Read Online

ACCESS | Metrics & More | Article Recommendations | Supporting Information

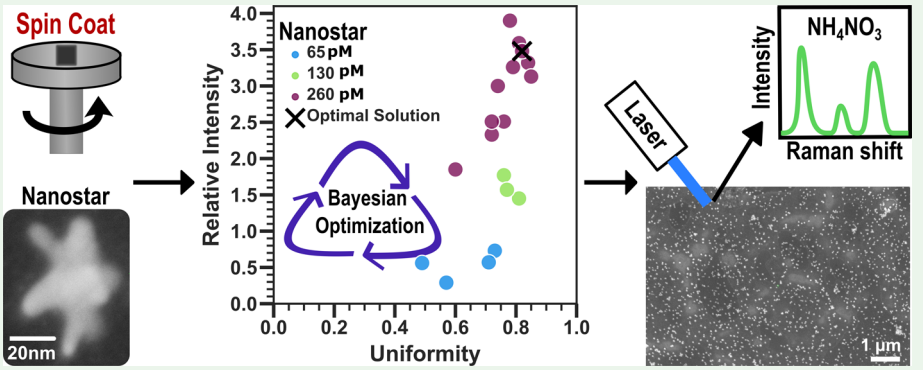

ABSTRACT: Field detection of trace analytes remains a challenge in many sectors, including national security, public health, and environmental monitoring. This challenge arises from the scarcity of field-deployable technologies capable of identifying trace analytes in the complex matrices of real-world samples. Surface-enhanced Raman scattering (SERS) is a promising technique for chemical sensing because it offers sensitive and specific analyte detection with commercial portable Raman systems. Despite the immense potential of SERS, commercially available SERS technologies that are accurate, reliable, cost-effective, and compatible with portable spectrometers remain scarce. This scarcity is due to the challenges associated with the complex design and resource-intensive optimization of the manufactured substrates that can achieve both high SERS intensity and signal uniformity. Machine learning (ML) tools are ideal for addressing complex optimization problems, but their application in SERS substrate fabrication remains largely unexplored. We present a pioneering example of applying ML to optimize SERS substrate fabrication using silver-coated gold nanostars for chemical sensing. In this study, we used multiobjective Bayesian optimization to achieve both high SERS intensity and signal uniformity across the SERS substrate. Optimal fabrication parameters were identified for spin and flow coating of silver-coated gold nanostars. The optimized spin coated substrate achieved an experimental limit of detection of 100 nM with an application relevant compound (ammonium nitrate), suggesting its potential for trace-level sensing. This work underscores the potential for ML to accelerate the development of field-deployable SERS technologies for trace analyte detection. Furthermore, we provide a general framework for optimized fabrication of nanoparticles on surfaces for other applications such as catalysis, electronics, and medicine.

KEYWORDS: *SERS, silver-coated gold nanostars, machine learning, multiobjective Bayesian optimization, ammonium nitrate, chemical sensor, flow coating, spin coating, Raman spectroscopy*

INTRODUCTION

The rapid and accurate field detection of trace analytes is of paramount importance in addressing critical challenges in national security, public health, and environmental monitoring.[1−4] Despite significant advancements in analytical techniques, the development of field-deployable technologies for trace analyte detection remains a significant challenge. Effective field-deployable technologies must be accurate, reliable, cost-effective, and user-friendly, capable of identifying minute quantities of analytes within real-world samples. Surface-enhanced Raman scattering (SERS) offers a potential solution by enhancing the intensity of analytes adsorbed onto metal

Received: March 10, 2025
Revised: May 5, 2025
Accepted: May 15, 2025

https://doi.org/10.1021/acsanm.5c01462
ACS Appl. Nano Mater. XXXX, XXX, XXX−XXX

nanoparticles,[5] making it both sensitive for trace analysis and specific due to their vibrational fingerprint. The SERS enhancement of analytes adsorbed on metal nanoparticles originates from the excitation of the localized surface plasmon resonance (LSPR) of the nanoparticle that is resonant with the Raman laser wavelength.[6] Additionally, the magnitude of the SERS enhancement depends on the nanoparticle morphology due to the varying number of hot spots (areas of localized electric field enhancement) on the nanoparticle surface. Anisotropic nanoparticle shapes, such as nanostars, have hot spots at the tip of every branch, providing significantly more enhancement than other shapes, such as rods with two hot spots.[7] The significant SERS enhancement observed from gold nanostars, with enhancement factors up to 10^9, has demonstrated detection of analyte concentrations in the femtomolar regime.[8]

Since the discovery of SERS over 50 years ago, this technique has flourished in fundamental laboratory research, demonstrating remarkable sensitivity down to single molecule detection using highly specialized nanofabricated substrates.[9] However, despite these achievements, it has struggled to transition from laboratory success to commercial chemical sensing applications. This is in part due to the lack of commercially available substrates that are accurate, reliable, cost-effective, and compatible with portable spectrometers.[10] Additionally, the analysis of real-world samples by nontechnical users remains an obstacle due to the complexity of spectral classification and analyte identification. These obstacles highlight the need for improved SERS substrates that can overcome the challenges of low analyte concentration, spectral interference, and signal variability. The complex design and resource-intensive optimization of SERS substrates, particularly in achieving both high SERS intensity and signal uniformity, pose significant obstacles to their widespread adoption.

To overcome the limitations of traditional SERS substrate optimization methods, machine learning (ML) offers a promising alternative. ML employs statistical methods to build models and make predictions, enabling efficient exploration of complex relationships with fewer experiments. This data-driven approach has the potential to significantly accelerate the development and optimization of SERS technologies. In the context of SERS, ML has demonstrated promise in two key areas.[10−12] First, ML classification tools can improve the accuracy of analyte identification and quantification in complex samples.[13−16] Second, ML algorithms can aid in the design of novel SERS substrates by predicting their plasmonic properties to overcome the challenges associated with traditional computational approaches.[17−20] By leveraging ML for both analyte identification and substrate design, researchers can pave the way for the development of SERS platforms with enhanced performance and broader applicability.

The fabrication of SERS substrates plays a crucial role in determining their performance and suitability for chemical sensing. Several techniques are commonly used for SERS substrate fabrication, each with its own set of advantages and limitations. Simple methods like drop-casting are rapid and easy to use; however, they suffer from poor reproducibility, making it difficult to assess the commercial viability of a substrate. In contrast, more sophisticated printing techniques, such as aerosol jet and inkjet printing, provide high reproducibility but their complexity can be cost prohibitive for initial exploration and prototyping. As an alternative, spin and flow coating techniques provide a valuable compromise between reproducibility and cost-effectiveness. These techniques offer greater control and consistency compared to drop-casting while remaining more accessible and less resource-intensive than printing methods. This makes them ideal for identifying promising SERS substrate prototypes before investing in more complex fabrication techniques. Despite their widespread use, there is a surprising lack of research utilizing ML to aid the optimization of spin and flow coating methods for SERS substrate fabrication. However, a growing body of literature demonstrates the successful application of ML for optimizing various printing[21−27] and fabrication processes[28−32] in related fields, such as electronics and photovoltaics. These successes suggest that ML holds significant promise for improving the efficiency and performance of SERS platforms for chemical sensing. To the best of our knowledge, no studies have explored this potential. This research gap presents a significant opportunity to leverage ML for optimizing these commonly used fabrication methods and demonstrate its ability to accelerate the development of SERS substrate prototypes.

In this study, we employed multiobjective Bayesian optimization (BO) to identify optimal fabrication parameters for spin and flow coating of silver-coated gold nanostars (Ag@AuNS). Our primary goal was to achieve high SERS intensity and signal uniformity, thereby improving sensing performance. To evaluate the performance of the optimized substrate, we selected two analytes with distinct characteristics: crystal violet (CV), a common dye used to evaluate SERS activity, and ammonium nitrate (AN), a substance relevant to security applications due to its presence in explosives. This study aimed to assess the ability of an open-source optimization algorithm to identify optimal SERS substrates using common fabrication methods. Overall, this study provides a framework for optimizing SERS substrate fabrication and enables researchers to efficiently evaluate the potential of new platform designs before investing significant resources in complex fabrication techniques.

EXPERIMENTAL SECTION

Materials. The following reagents and reagent-grade solvents were purchased from Sigma-Aldrich: (3-aminopropyl)triethoxysilane (APTES), Tween 20, crystal violet, NH_4NO_3, isopropanol, ethanol, acetone, $HAuCl_4$, HCl, $AgNO_3$, NH_4OH, ascorbic acid (AA), and PEG-SH (MW 5K). A Millipore water purification system provided 18 MΩ DI H_2O.

Silver-Coated Gold Nanostar Synthesis. Ag@AuNS were synthesized using a seed-mediated approach reported previously.[33] First, gold nanoparticles (seeds) were synthesized following a modified Turkevich method.[34] In brief, 100 mL of 1 mM $HAuCl_4$ was stirred and boiled in a 250 mL Erlenmeyer flask. The gold solution was reduced with 15 mL of 1% (w/v) trisodium citrate solution and continued to stir and boil for 30 min, while maintaining a constant volume. The resulting gold seeds, a deep red solution, was cooled to room temperature, then vacuum-filtered with a 0.22 μm nitrocellulose membrane and stored 4 °C.

Second, the Ag@AuNS were synthesized at room temperature, under stirring, 10 mL of DI H_2O, 10 μL 1 N HCl, and 493 μL of 5.08 mM $HAuCl_4$ were added sequentially to a plastic scintillation vial. Next, 100 μL of gold seeds (12 nm) were added, followed by quickly adding 50 μL of 2 mM $AgNO_3$ and 50 μL of 0.1 M AA. The solution turned from a pale pink to a blue. After 30 s, 50 μL of 0.1 M $AgNO_3$, quickly followed by 10 μL of 29% NH_4OH were added. The solution turned from blue to red-brown. The reaction was stirred for an additional 2 min to stabilize the reaction, then transferred and allowed to incubate, idle at room temperature for 2 h. Later, the Ag@AuNS were concentrated by centrifugation in 5.5 mL aliquots at 1500g, 15 min, 4 °C. The

https://doi.org/10.1021/acsanm.5c01462
ACS Appl. Nano Mater. XXXX, XXX, XXX−XXX

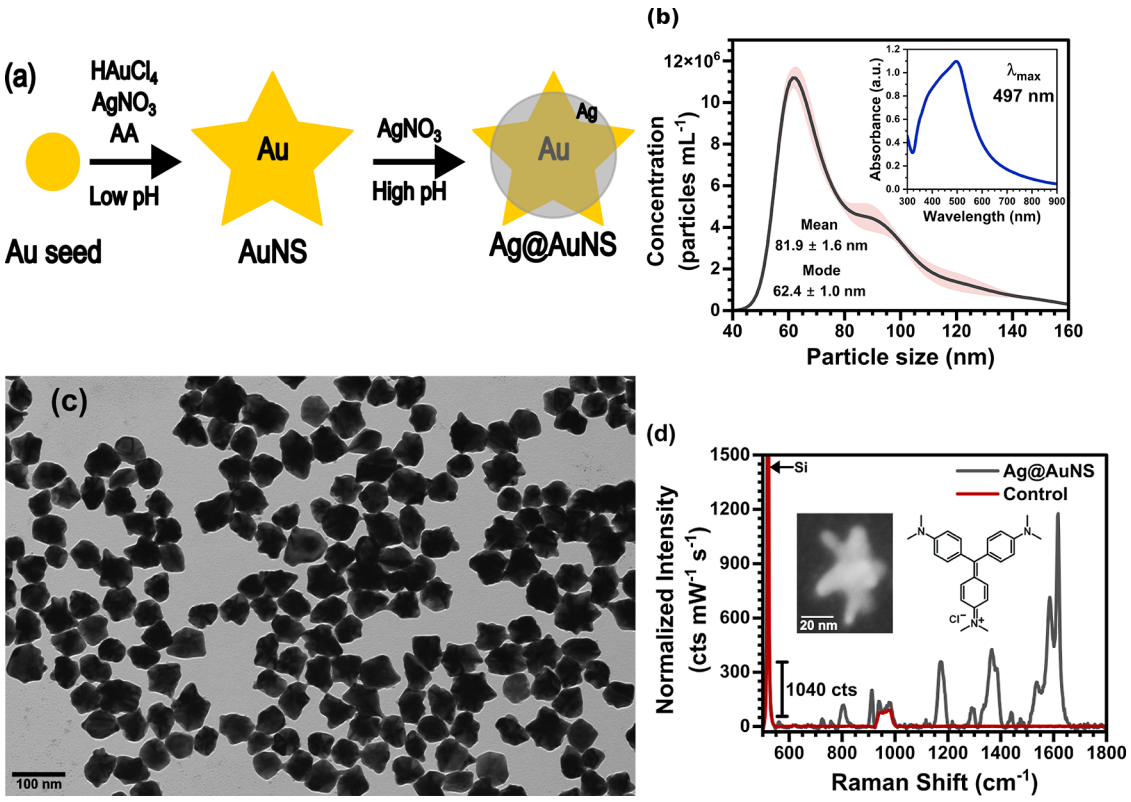

Figure 1. Synthesis, characterization and SERS activity of Ag@AuNS. (a) Synthetic scheme for Ag@AuNS, where AA stands for ascorbic acid. (b) Nanoparticle tracking analysis shows the particle size distribution and concentration of synthesized Ag@AuNS. The absorption spectrum in the inset indicates a LSPR peak at 497 nm. (c) TEM image of Ag@AuNS confirms their size and heterogeneous composition, indicative of successful silver coating on gold nanostars. (d) SERS activity of Ag@AuNS evaluated using 1 mM CV and 488 nm laser excitation. The main panel shows the enhanced Raman signal of CV obtained with the Ag@AuNS substrate compared to the control silicon substrate. The insets displaying the structure of CV and a high-resolution SEM image of an Ag@AuNS, highlighting its morphology.

supernatant was removed, and the pellets were redispersed with fresh DI H_2O to create a 10x concentrated Ag@AuNS solution, which was stored at 4 °C.

Characterization. *Optical Measurements.* For the UV−vis measurement, a BioTek Synergy HTX microplate reader measured the absorbance from 300 to 900 nm. A NanoSight NS300 (Malvern) nanoparticle tracking analysis system with a 532 nm laser was used to measure the hydrodynamic diameter and concentration of Ag@AuNS. We diluted the samples 200 times in DI H_2O prior to the measurement.

Electron Microscopy. For TEM measurements of nanoparticles, Ag@AuNS were treated with PEG-SH (final concentration 90 μM) for 30 min to stabilize the surface. Next, the Ag@AuNS were washed with DI H_2O at 4000g for 10 min at 4 °C. The supernatant was removed, and fresh DI H_2O was used to redisperse the cleaned Ag@AuNS. Ten μL of this solution was dispensed on a Formvar/Carbon 200 Mesh, Copper grid, and allowed to dry overnight. The Ag@AuNS grid was imaged with a Hitachi HT7800 TEM at 80 kV, and images were collected using AMT V702 software with a BIOSPR16 camera.

SEM analysis was performed on a ZEISS (Germany) Gemini 500 with an accelerating voltage of 3−5 kV and a working distance of 3−8 mm for imaging with an in-lens detector. EDS measurements were performed with an Oxford Instruments (United Kingdom) X-Max detector with an accelerating voltage of 5 kV at a working distance of 5−8 mm.

SERS Measurements. Measurements were taken on a Renishaw inVia Raman microscope using a 488 nm laser. We drop casted 5 μL of 1 mM CV in isopropanol on each substrate and allowed to dry overnight. Five Raman maps were then collected over a 405 μm^2 area per sample. Each map was 9 × 9 μm with a 3 μm spacing and each map spaced 100 μm apart. This resulted in 80 spectra for each substrate. Acquisition parameters were set to 10 s exposure at 5% power (57 μW) and 1 accumulation. For enhancement factor and limit of detection substrates, normalized intensity was calculated by dividing the spectrum counts by the product of the laser power, exposure time, and number of accumulations.

SERS Substrate Fabrication. *Substrate Preparation.* Silicon wafers were cut into squares (8 mm^2) for spin coating and 5 × 3 cm rectangles for flow coating. The Si wafers were cleaned in a sonication bath (Branson 1510) for 5 min in acetone followed by 5 min in isopropanol, then blown dry with nitrogen and placed in a UV Ozone system (Novascan PSD Pro Series) for 10 min. Clean Si wafers were placed in a fresh 10% (v/v) APTES in ethanol and incubated at 70 °C for 1 h. After cooling to room temperature, the substrates were rinsed 3 times with DI water, then 3 times with ethanol. The substrates were stored in ethanol and dried with nitrogen before use. To concentrate the Ag@AuNS, particles were centrifuged at 4000*g* for 20 min. Half of supernatant was then removed, and the solution was vortexed. This process was repeated until desired concentration was reached. To prevent clumping, Tween 20 in DI water was added to Ag@AuNS solution for a total concentration of 0.01% (v/v) Tween 20 prior to centrifugation.

Substrate Coating. For spin coated substrates, a Laurell model WS-650-Lz-23NPPB spin coater was used with a static dispense of 5 μL of Ag@AuNS and a two-step program consisting of an initial step at 500 rpm with an acceleration of 500 rpm for 30 s, followed by a second step at the desired speed (rpm) with a 120 s dwell time and an acceleration of 500 rpm. Flow coated substrates were prepared using a custom-built apparatus with a 4 mm wide quartz blade and 1.5 mm blade gap. Ten μL of the Ag@AuNS were placed under the blade, and the blade was moved after 1 min at the desired blade velocity (mm s^{-1}). Before each coating procedure, the Ag@AuNS were allowed to warm up to room temperature and vortexed. Stock solutions of CV (1 M in isopropanol) and AN (1 M in DI water) were prepared and diluted to the desired concentration for analyte detection. We drop casted 5 μL of the analyte

https://doi.org/10.1021/acsanm.5c01462
ACS Appl. Nano Mater. XXXX, XXX, XXX−XXX

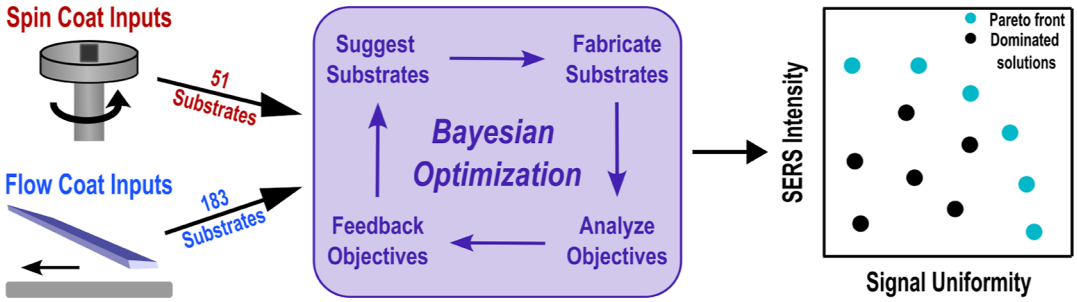

Figure 2. Workflow for the multiobjective BO of SERS substrate fabrication. This diagram illustrates the iterative process used to optimize the fabrication of SERS substrates via spin and flow coating. The optimization begins by defining a design space encompassing all possible combinations of the fabrication parameters (concentration of Ag@AuNS and spin speed or blade velocity). Subsequently, the algorithm suggests substrates for preparation. The substrates are characterized and their SERS intensity and signal uniformity are analyzed. Lastly, the results are fed back into the BO algorithm. This iterative process continues until an optimal solution is found. The objective plot on the right illustrates the substrates prepared throughout the optimization with the teal points indicating the Pareto front.

onto the substrate and allowed to dry overnight before analysis. Control substrates on Si substrates were prepared as described above.

Bayesian Optimization. For SERS substrate fabrication optimization, we used the experimental design via BO (EDBO+) tool, an open-source platform for multiobjective Bayesian reaction optimization, recently developed by Doyle and co-workers.[35] EDBO+ can be accessed through its web application[36] or the source code can be downloaded from Github.[37] The design space fabrication parameters (inputs) and objectives (outputs) can be found in Table S1. The CVT sampling method was used to suggest substrates for the first round of the optimization campaign.

Data Analysis. The Raman spectra were processed using asymmetrically reweighted penalized least-squares baseline subtraction algorithm, fit with a pseudo-Voigt line shape, and the average relative intensity, I_{CV}/I_{Si}, was calculated for each substrate in Python. For each substrate, the relative standard deviation (RSD) was calculated from the mean and standard deviation of the relative intensity across 80 spectra. Signal uniformity was defined as 1-RSD, ranging from 0 (not uniform) to 1 (uniform). We used Python to perform the optimization analysis, including calculations for the Pareto front, hypervolume indicator, objective convergence, and expected hypervolume improvement. The Pymoo[38] package was used to calculate the hypervolume indicator. Since the Pymoo package only minimizes objectives, we used the negative of both objectives with a reference point of (0,0) to calculate the hypervolume indicator, effectively maximizing both objectives. To generate the objective convergence plots, we identified the maximum objective value for each round, considering the value from that round and all preceding rounds. For instance, for round 2, we combined the data for rounds 1 and 2 before determining the maximum value. For each round after the initial round, EDBO+ calculated and reported the maximum expected hypervolume improvement values as a csv file. We extracted the maximum expected hypervolume improvement values from the suggested substrates in that round for each objective.

RESULTS AND DISCUSSION

Figure 1a illustrates the two-step synthesis of Ag@AuNS: first, gold nanostars were synthesized from gold nanoparticle seeds; second, a silver coating was added to the gold nanostars. The Ag@AuNS were characterized using a combination of techniques to assess their LSPR, size, morphology, and composition. The absorption spectrum (Figure 1b inset) showed a broad LSPR peak at 497 nm, which was essential for SERS activity. Nanoparticle tracking analysis determined the mean Ag@AuNS size to be 81.9 ± 1.6 nm with a mode of 62.4 ± 1.0 nm and an average final concentration of slightly below 7.9×10^{10} particles mL^{-1} (Figure 1b). This size distribution was confirmed by TEM imaging (Figures 1c and S1), which also revealed the heterogeneity of the Ag@AuNS, confirming the successful coating of gold nanostars with silver. The presence of both Ag and Au in the composition of the nanostars was further confirmed by EDS (Figure S2). Finally, high-resolution SEM imaging (Figure 1d inset) confirmed the characteristic star shape of the nanoparticles. These characterization results confirmed the successful synthesis of Ag@AuNS.

To evaluate the SERS activity of the Ag@AuNS, we used 1 mM CV, a standard dye commonly employed for this purpose. Based on the LSPR peak at 497 nm (Figure 1a inset), we selected a 488 nm laser for our SERS measurements to maximize the excitation of surface plasmons. Figure 1d shows the SERS spectra of CV (structure shown in Figure 1d inset) adsorbed on Ag@AuNS. The two most intense Raman modes for CV, at 1585 cm^{-1} and 1615 cm^{-1} correspond to the in-plane and out-of-plane C−C phenyl stretching, respectively. The Ag@AuNS exhibit clear SERS activity, as evidenced by the enhancement of the CV signal compared to 1 mM CV on a control silicon substrate.

SERS Substrate Optimization. To efficiently optimize the SERS substrates, we employed multiobjective BO, an ML algorithm that optimizes multiple objectives to identify the best set of solutions. This approach is well-suited for field sensing where data must be acquired rapidly and reliably. Thus, maximizing both SERS intensity and signal uniformity across the substrate are crucial for reliable field measurements. In our study, we used the EDBO+ algorithm[35] to optimize the SERS intensity and signal uniformity across the substrate. This open-source algorithm constructs a probabilistic surrogate model through iterative exploration of the design space, guided by an acquisition function.[39] Although EDBO+ was initially developed for optimizing chemical reactions, the "black-box" nature of BO allows it to be applied to a wide variety of optimization problems,[39] including the fabrication of SERS substrates.

Figure 2 outlines the workflow for the spin and flow coating optimization. The goal of this optimization was to identify the fabrication parameters (inputs) that yield SERS substrates with both high SERS intensity and signal uniformity (outputs) within the design space. As shown in Figure 2, we began by defining the design space, which encompasses all possible substrates based on the inputs. These inputs were the Ag@AuNS concentration ([Ag@AuNS]) and spin speed (rpm) or blade velocity (mm s^{-1}) for spin and flow coating, respectively. To conserve Ag@AuNS in this proof-of-concept optimization, we limited the design space by placing constraints on inputs, as detailed in Table S1. The design spaces contained 51 and 183 possible substrates for spin and flow coating, respectively.

https://doi.org/10.1021/acsanm.5c01462
ACS Appl. Nano Mater. XXXX, XXX, XXX−XXX

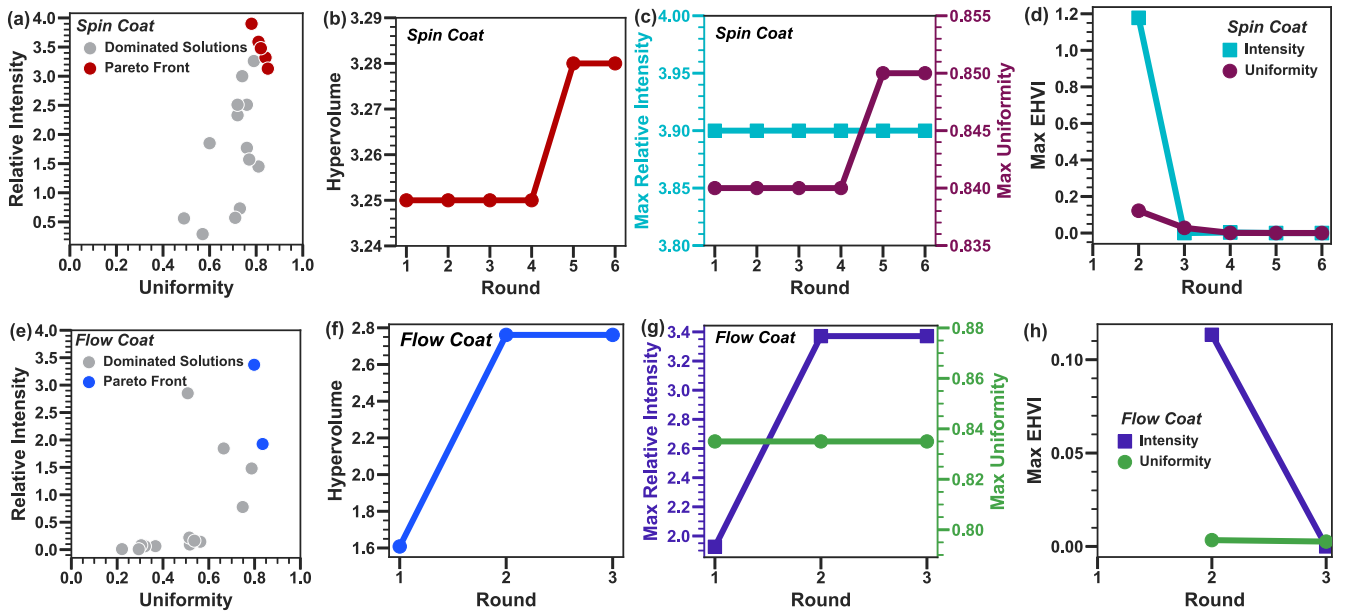

Figure 3. Analysis of the BO campaigns for spin and flow coating fabrication methods. The objective plots for spin (a) and flow (e) coating illustrate the dominated (gray) and Pareto front solutions (colored). The convergence of the campaigns was evaluated using the HV indicator, objective convergence plots, and the EHVI. The HV indicator (b,f) is the area under the Pareto front per round, which increases until the optimization converges. Objective convergence plots (c,g) show the cumulative maximum relative intensity and uniformity achieved in each round, indicating optimization convergence after both objectives plateau. The EHVI plots (d,h) illustrate the predicted objective improvement per round, decreasing as the optimization converges.

As illustrated in Figure 2, each optimization round consisted of four steps: (1) EDBO+ suggested substrates for preparation, (2) the substrates were fabricated and characterized, (3) ML objectives were analyzed, and (4) the objectives were fed back into EDBO+ for the next round of suggestions. First, EDBO+ suggested a set of substrates based on the desired optimization objectives and the batch size. The batch size, i.e. the number of substrates evaluated in each round, was chosen to balance the time required for each round with the need to efficiently explore the design space. We chose a batch size of 3 substrates for the spin coating campaign and 5 substrates for the flow coating campaign, covering 6% and 3% of the design space per round, respectively. Next, we spin or flow coated the Ag@AuNS onto silicon substrates using the specified fabrication parameters. Using 1 mM CV as the analyte, we measured the SERS spectra of each substrate and analyzed them to determine the SERS intensity and signal uniformity. To prevent the optimization from biasing SERS intensity over signal uniformity, we ensured that the values for both objectives were of similar magnitudes. This was achieved by defining a relative SERS intensity (I_{CV}/I_{Si}) as the ratio of the CV peak intensity at 1615 cm^{-1} to the silicon peak intensity at 520 cm^{-1}, scaling the SERS intensity values between 0 and 5. The signal uniformity was defined as 1-RSD, where values closer to 1 indicate high uniformity. Finally, the objectives (relative intensity and uniformity) were fed back to EDBO+ to complete the round. EDBO+ then used these objectives to suggest the next set of substrates, and the entire process was repeated until the optimization was complete. The objective plot on the right summarizes all the fabricated substrates (solutions) by plotting relative intensity versus uniformity. The black points represent the dominated solutions, a subset of solutions with low values for one or both objectives. The teal points in the objective plot visualize the Pareto front, which are a subset of nondominated solutions, that contains the optimal solution for the campaign.[40]

To assess the progress and convergence of the optimization campaigns, we analyzed the objectives after each round using the hypervolume (HV) indicator, objective convergence, and expected hypervolume improvement (EHVI). The objective plots for spin (Figure 3a) and flow (Figure 3e) coating represent the relative intensity and uniformity values for all substrates analyzed (solutions) during the campaign. In the objective plots, the optimization solutions (substrates) can be divided into two categories: dominated and nondominated solutions. The set of nondominated solutions represents the best substrates in terms of the desired objectives (high SERS intensity and signal uniformity) and form the Pareto front. The Pareto fronts are represented using red or blue in Figure 3a,e, and the dominated solutions are represented in gray. To monitor the progress of the campaign, we calculated the Pareto front and analyzed the HV indicator after each round. The HV is the area under the Pareto front, which increases as the campaign explores the design space and expands the Pareto front. The HV indicator tracks the HV to quantify this area with respect to a reference point. As the campaign progresses, the HV indicator reaches a maximum and plateaus, indicating that further rounds of the campaign are unlikely to identify solutions beyond the Pareto front. For the spin coating campaign, the HV indicator reached a maximum at round 5 and plateaued by round 6 as shown in Figure 3b. In the flow coating campaign, the HV indicator reached a maximum at round 2 and plateaued by round 3 (Figure 3f). The plateau of the HV indicator suggests the convergence of the optimization has been reached.

Another metric for assessing the progress of the campaign is tracking the convergence of the objective values as shown in Figure 3c,g. These plots illustrate the cumulative maximum values for the relative intensity and uniformity (left and right axes, respectively) during each round of the campaign. For example, in Figure 3c, the maximum relative intensity is 3.9 in round 1 (3 substrates). If we consider the combined relative

https://doi.org/10.1021/acsanm.5c01462
ACS Appl. Nano Mater. XXXX, XXX, XXX−XXX

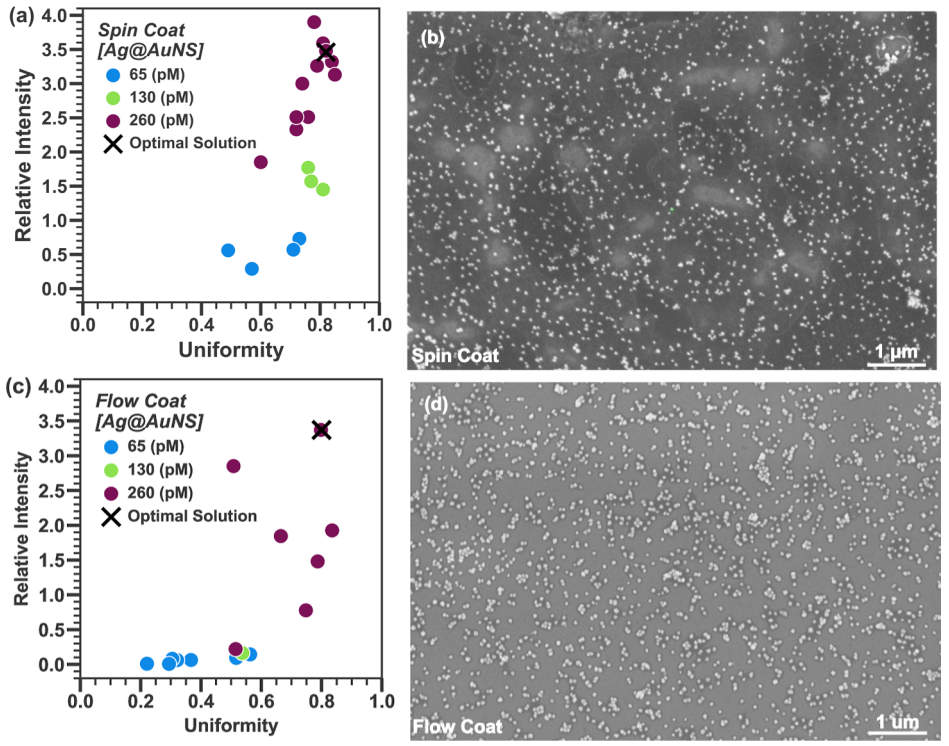

Figure 4. Experimental objective plots colored by concentration of nanostars ([Ag@AuNS] pM) for the (a) spin coating and (c) flow coating campaigns, with the optimal substrates marked with an "x". SEM images of (b) spin coating and (d) flow coating optimal substrates.

intensities from rounds 1 and 2 (6 substrates), the maximum value is still 3.9 (achieved during round 1). If we consider all 6 rounds (18 substrates), the maximum relative intensity is still 3.9 that was achieved during round 1. Interestingly, the spin coating campaign discovered the maximum relative intensity in the first round but took until round 5 to find the maximum uniformity. Both objectives converged at their maximum value during round 5, which is consistent with the HV indicator reaching a maximum value at round 5 (Figure 3b). In contrast, the flow coating campaign found the maximum uniformity during round 1 and the maximum relative intensity in round 2. Similar to the spin coating campaign, the objective convergence is consistent with the HV indicator (Figure 3f), both reaching their maximum values during round 2.

Lastly, we monitored the EHVI that is derived from the surrogate model. The EHVI predicts the potential objective improvement in the subsequent campaign round. As the optimization advances toward convergence, the maximum EHVI for each objective diminishes to a minimum value. In essence, the convergence of EHVI for both objectives suggests that further campaign rounds are unlikely to yield significant objective improvement. Figure 3d,h show the maximum EHVI predicted for each objective during a campaign round. For instance, in Figure 3d, the surrogate model predicted a maximum improvement of the relative intensity of 1.2 during round 2 of the spin coating campaign. Following round 2, the optimization did not identify a substrate with a relative intensity value higher than discovered in round 1 (Figure 3c: 3.9). After feeding back the objective values for round 2 into the optimization, the surrogate model updates and predicts a negligible improvement ($\ll 1$) for relative intensity for round 3, as no improvement was observed in round 2. We observed a decrease in the maximum EHVI values for both objectives as the campaigns progressed, reaching a minimum at round 5 for spin coating and round 3 for flow coating. The observed minimization of EHVI supports the campaign completion. Based on the analysis of the HV indicator, objective convergence, and EHVI, we concluded that both optimization campaigns had reached convergence. Tables S2 and S3 summarize the fabrication parameters (inputs) and respective objectives (outputs) for each optimization campaign.

With the goal of achieving high SERS intensity and signal uniformity across the substrate, we proceeded to select the optimal solution for each fabrication method from the Pareto front. Although the Pareto front presented multiple substrates, the selection of the optimal substrates was guided by SEM imaging. The optimal substrates for the spin and flow coating campaigns are marked with an "x" in Figure 4a,c, respectively, and summarized in Table 1. Figure 4a,c present the same data as in Figure 3a,e, but the solutions are colored by the concentrations of the Ag@AuNS. These optimal substrates exhibited a fairly uniform distribution of particles with some aggregation, as shown in the SEM images (Figure 4b,d). To quantify the optimization performance, we calculated an

Table 1. Optimal Spin and Flow Coating Parameters (Inputs) and Corresponding SERS Performance Objectives (Outputs) Identified via BO[a]

	spin coating campaign	flow coating campaign
Ag@AuNS (pM)	260	260
spin speed or blade velocity	2250 rpm	0.1 mm s^{-1}
relative intensity	3.48	3.37
uniformity	0.82	0.80
acceleration metric	1.6×	8.8×

[a]The acceleration metric compares the time taken by the campaign to find the optimal substrate with the average time for a random selection to find it over 100 trials.

https://doi.org/10.1021/acsanm.5c01462
ACS Appl. Nano Mater. XXXX, XXX, XXX−XXX

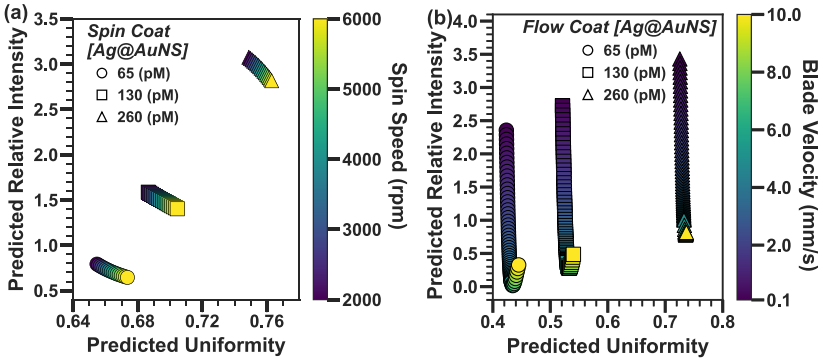

Figure 5. Analysis of predicted objective plots for spin and flow coating optimizations derived from the surrogate models. Predicted objective plots for (a) spin coating and (b) flow coating, where marker color represents the spin speed or blade velocity, respectively. The concentration of nanostars ([Ag@AuNS] pM) is represented by marker shape.

acceleration metric that compared the time required for EDBO+ to identify the optimal substrate to the average time to find the optimal solution randomly through 100 trials. The acceleration metrics were 1.6× and 8.8× for spin and flow coating optimizations, respectively. The "black-box" nature of BO does not allow for much insight into the differences in the acceleration metrics, but nevertheless, both optimizations identified the optimal substrate faster than selecting parameters randomly.

As can be seen in Figure 4a,c, there is a clear dependence on [Ag@AuNS], with higher concentrations generally yielding higher relative intensity and uniformity. To further analyze this relationship, we evaluated the predicted objective plots (Figure 5) derived from the surrogate model constructed during the optimization campaign. The surrogate model describes the relationship between the input variables ([Ag@AuNS] and spin speed or blade velocity) and the campaign objectives (relative intensity and uniformity). This relationship is quantified through hyperparameter values in the surrogate model describing each input variable (Θ_{input}), where smaller values indicate a greater contribution to the campaign objective. The hyperparameter values generated from the surrogate models are in Tables S4 and S5. From the surrogate model, we can construct the predicted objective plots for all input variables. Figure 5 plots the campaign objectives against [Ag@AuNS] (indicated by marker shape) and spin speed or blade velocity (indicated by marker color) for each fabrication method.

For spin coating, the concentration of Ag@AuNS has a greater predicted contribution to both campaign objectives when compared to the spin speed. These contributions are more clearly illustrated in the predicted objective plot (Figure 5a) and hyperparameter values (Table S4) generated from the surrogate model. For flow coating, the concentration of Ag@AuNS contributed more to the uniformity, while the blade velocity contributed more to the relative intensity. These trends are summarized in the predicted objective plot (Figure 5b) and the hyperparameter values (Table S5) generated from the surrogate model. Ideally, the surrogate model would provide valuable insights into the underlying physics dictating the relationship between the input variables and output objectives. The interpretability of ML-based predictions remains a significant challenge due to the black-box nature of these approaches. Current research efforts to develop explainable artificial intelligence models could provide the transparency required to provide valuable insights into the underlying physics.[41]

Although the surrogate model predictions lack interpretability, we assessed the accuracy of the predictions with our experimental data (Figure S3). In comparing the experimental data to the predictions, we observed moderate scatter in the data. We hypothesize that the simplified fabrication parameters used in this proof-of-concept study did not capture the entire landscape required for accurate prediction. Spin and flow coating are complex processes influenced by various factors, including environmental conditions and stochastic nature of manual processes. This complexity can impede reproducibility of the results, especially with benchtop apparatuses and manual operation. To improve the accuracy of the surrogate models, future work could explore combining BO with automated, robotic, or commercial manufacturing equipment, as this approach has shown promise in accelerating prototype development in other fields.[22,29] Nonetheless, our study demonstrates the value of utilizing BO for optimizing SERS substrate prototypes. Moreover, the general framework presented here can be extended to the optimized fabrication of nanoparticles on surfaces for various applications beyond SERS, such as catalysis, electronics, and medicine.

SERS Substrate Performance. To benchmark the performance of the optimized spin coated SERS substrate, we evaluated the analytical enhancement factor (EF), the limit of detection (LOD) and substrate stability. The analytical EF quantifies the signal enhancement achieved by the SERS substrate compared to a control substrate. It can be expressed as

$$\mathrm{EF} = \frac{I_{\mathrm{SERS}} C_{\mathrm{Raman}}}{I_{\mathrm{Raman}} C_{\mathrm{SERS}}}$$

where I_{SERS} and I_{Raman} are the analyte intensities on the SERS substrate and control substrate, respectively, and C_{SERS} and C_{Raman} are the corresponding analyte concentrations.[42] Control experiments with CV and AN (Figure 6) demonstrate the SERS enhancement of the optimal spin coated substrate. The Raman spectra of powder CV and AN are shown in Figure S4. The most intense peaks were used for EF calculations, with a peak around 1615 cm^{-1} for CV (out-of-plane C−C phenyl stretching) and at 1050 cm^{-1} (symmetric stretch of NO_3^-)[43] for AN. The average analytical EFs were 1.4×10^5 for CV and 2.3×10^5 for AN. We acknowledge these EFs are lower than previously reported for other gold nanostars, with EFs up to 10^9.[8] We hypothesize that the lower EFs for our Ag@AuNS are related to the lower nanostar branch density as compared with other gold nanostars reported in the literature, resulting from different synthetic conditions, leading to fewer hot spots for SERS enhancement.

https://doi.org/10.1021/acsanm.5c01462
ACS Appl. Nano Mater. XXXX, XXX, XXX−XXX

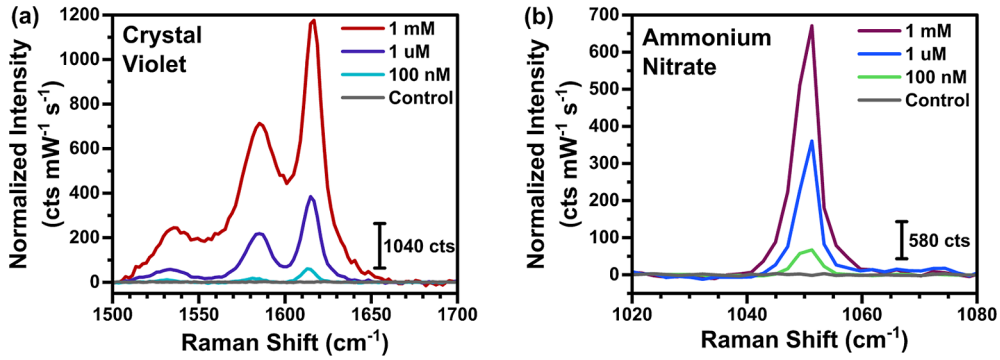

Figure 6. SERS performance of the optimal spin coated Ag@AuNS substrate with CV (a) and AN (b) using 488 nm laser excitation. An experimental LOD of 100 nM was achieved for both analytes, demonstrating the high sensitivity of the optimized substrate. The control substrate was 1 mM of the respective analyte on silicon.

For the purpose of this study, we aimed to illustrate the ability of BO to identify the optimal substrate within the design space; therefore, the EF of the nanostars was not critical to testing the BO algorithm. We hypothesize that the BO algorithm would be able to identify the optimal substrate in that design space using nanostars with larger EFs; this is the subject of ongoing work but this is beyond the scope of this study.

The LOD was evaluated for CV and AN by measuring the SERS intensity of analyte concentrations ranging from 1 mM - 1 nM on the optimized spin coated substrate. The experimental LOD was determined as the lowest analyte concentration for which the signal was distinguishable from the background noise. As shown in Figure 6, the average experimental LOD for both CV and AN was 100 nM. This experimental LOD, representing the lowest detectable concentration, is distinct from a calculated LOD derived from a calibration curve. Our substrate exhibited comparable SERS performance to other laboratory-prepared substrates for both analytes (Table S6). To the best of our knowledge, Kumar and Soni reported the lowest AN LOD to date, with an experimental LOD of 100 nM and a calculated LOD of 31 nM with drop-casted Ag triangular nanoplates.[44] Achieving the same experimental LOD of 100 nM for AN using our optimal spin coated substrate demonstrates the validity of BO for attaining comparable SERS performance as traditional methods. Lastly, we evaluated the stability of the spin coated substrate at 65 and 234 days after initial fabrication with CV. Figure S5 shows a slight decrease in the relative intensity and uniformity with time. The relative intensity decreases by 11% (day 65) and 17% (day 234) but is within the standard deviation (error bar) of the measured intensities. The standard deviations increase with time, causing a decrease in the uniformity of the substrate by 14% (day 65) and 19% (day 234). The stability performance of the substrate shows it should be used within 2 months.

Future work to expand the campaign design space to increase the Ag@AuNS concentration range could yield SERS substrates with lower LODs (higher sensitivity), but we hypothesize that the SERS intensity will eventually saturate, placing a limit on the substrate sensitivity achieved for that fabrication method. This effect has been reported in the literature for aerosol jet printed of Ag nanoparticles, where the SERS intensity increased with each print pass up until 4 print passes, then decreased SERS intensity with 5 and 6 print passes.[45] Crucially, our study shows that BO is well poised to identify parameters that produce the maximum SERS intensity possible with the lowest concentration of SERS-active nanoparticles. This will potentially yield highly sensitive, yet cost-effective SERS substrates for chemical sensing, but is beyond the scope of this study.

Translating of SERS performance from laboratory-prepared substrates to commercial substrates is crucial for trace analyte field detection. Liszewska et al. evaluated three commercial substrates using portable Raman systems and reported 1 mM experimental LODs for AN,[46] highlighting the performance gap between current commercially available and laboratory-prepared substrates (Table S6). There are several potential avenues for BO to bridge this gap, such as expanding the design space, incorporating automated fabrication platforms, or extending to more complex fabrication methods (e.g., inkjet printing) to consider in future work. Nevertheless, BO has the potential to accelerate the development of commercial SERS platforms for portable trace analysis.

CONCLUSION

The development of accurate, reliable, and cost-effective SERS technologies remains a critical challenge for trace analyte field detection in real-world samples, inhibiting widespread adoption. ML tools offer a promising avenue for overcoming these challenges through synergistic optimization of analyte identification and substrate design. To evaluate the potential for ML-guided SERS substrate fabrication, we employed a multiobjective BO tool, EDBO+, to optimize the SERS intensity and signal uniformity of Ag@AuNS substrates via spin and flow coating methods. Our optimized substrates exhibited excellent SERS performance, achieving an average analytical EF of 1.4×10^5 for CV and 2.3×10^5 for AN, with an experimental LOD of 100 nM for both analytes. Notably, the 100 nM experimental LODs highlight the potential for BO to identify SERS prototypes with sensitivity for trace-level detection of explosives for national security. By demonstrating the successful application of a multiobjective BO algorithm to optimize common substrate fabrication methods, we provide researchers with an easy-to-use, open-source BO tool to accelerate the development of SERS technologies. Building on this foundation, future studies can explore the application of ML optimization techniques to more complex fabrication methods, such as inkjet printing, or by integrating automated fabrication methods to pave the way for the reproducible, large-scale manufacturing of high-performance SERS platforms for chemical sensing. Moreover, the general framework presented in this study can be extended to optimize the fabrication of nanoparticles on surfaces for various applications beyond SERS, including catalysis, electronics, and medicine.

https://doi.org/10.1021/acsanm.5c01462
ACS Appl. Nano Mater. XXXX, XXX, XXX−XXX

■ ASSOCIATED CONTENT

Supporting Information

The Supporting Information is available free of charge at https://pubs.acs.org/doi/10.1021/acsanm.5c01462.

The Supporting Information includes TEM images, EDS spectra, optimization design space table, BO campaign inputs/outputs tables, BO surrogate model hyperparameters tables, experimental objective plots, powder spectrum for CV and AN, SERS performance comparison table, and optimal substrate stability data (PDF)

■ AUTHOR INFORMATION

Corresponding Authors

Andrea N. Giordano − *Materials and Manufacturing Directorate, Air Force Research Laboratory, Wright-Patterson Air Force Base 45433 Ohio, United States; National Research Council, Washington 20001 District of Columbia, United States;* orcid.org/0000-0001-6668-7747; Email: andrea.giordano.2.ctr@us.af.mil

Rahul Rao − *Materials and Manufacturing Directorate, Air Force Research Laboratory, Wright-Patterson Air Force Base 45433 Ohio, United States*; Email: rahul.rao.2@us.af.mil

Authors

Samuel Franqui-Rios − *Materials and Manufacturing Directorate, Air Force Research Laboratory, Wright-Patterson Air Force Base 45433 Ohio, United States;* orcid.org/0009-0000-5471-6985

Steven M. Quarin − *Department of Chemistry, University of Cincinnati, Cincinnati 45221 Ohio, United States;* orcid.org/0009-0005-3309-372X

Der Vang − *Department of Chemistry, University of Cincinnati, Cincinnati 45221 Ohio, United States;* orcid.org/0000-0002-2884-805X

Drake R. Austin − *Materials and Manufacturing Directorate, Air Force Research Laboratory, Wright-Patterson Air Force Base 45433 Ohio, United States;* orcid.org/0000-0003-0178-3791

Abigail G. Doyle − *Department of Chemistry & Biochemistry, University of California, Los Angeles 90095 California, United States;* orcid.org/0000-0002-6641-0833

Luke A. Baldwin − *Materials and Manufacturing Directorate, Air Force Research Laboratory, Wright-Patterson Air Force Base 45433 Ohio, United States;* orcid.org/0000-0002-7787-238X

Pietro Strobbia − *Department of Chemistry, University of Cincinnati, Cincinnati 45221 Ohio, United States;* orcid.org/0000-0003-0884-6185

Complete contact information is available at: https://pubs.acs.org/10.1021/acsanm.5c01462

Notes

The authors declare no competing financial interest.

■ ACKNOWLEDGMENTS

A.N.G, L.A.B, and R.R acknowledge support from the Air Force Research Laboratory Materials and Manufacturing Directorate. Additionally, A.N.G acknowledges support in part by the appointment to the NRC Research Associateship Program administered by the Fellowships Office of the National Academies of Sciences, Engineering, and Medicine. At the Air Force Research Laboratory, the authors thank John H. Dunlap and Amanda A. Volk for assistance with EDBO+, Keyna Hazell for assistance operating the flow coater, and Melinda Ostendorf (Materials Characterization Facility) for assistance with the SEM/EDS data. At the University of Cincinnati, the authors thank Melodie A. Fickenscher at the Advanced Material Characterization Center for help and advice on TEM characterization. Lastly, the authors thank Lyndsay Kissell for initial nanostar synthesis and advice on substrate preparation.

■ REFERENCES

(1) Hakonen, A.; Andersson, P. O.; Stenbæk Schmidt, M.; Rindzevicius, T.; Käll, M. Explosive and chemical threat detection by surface-enhanced Raman scattering: A review. *Anal. Chim. Acta* **2015**, *893*, 1−13.

(2) Ateia, M.; Wei, H.; Andreescu, S. Sensors for Emerging Water Contaminants: Overcoming Roadblocks to Innovation. *Environ. Sci. Technol.* **2024**, *58*, 2636−2651.

(3) Rodriguez, R. S.; O'Keefe, T. L.; Froehlich, C.; Lewis, R. E.; Sheldon, T. R.; Haynes, C. L. Sensing Food Contaminants: Advances in Analytical Methods and Techniques. *Anal. Chem.* **2021**, *93*, 23−40.

(4) Sohrabi, H.; Bolandi, N.; Hemmati, A.; Eyvazi, S.; Ghasemzadeh, S.; Baradaran, B.; Oroojalian, F.; Reza Majidi, M.; de la Guardia, M.; Mokhtarzadeh, A. State-of-the-art cancer biomarker detection by portable (Bio) sensing technology: A critical review. *Microchem. J.* **2022**, *177*, 107248.

(5) Fleischmann, M.; Hendra, P. J.; McQuillan, A. J. Raman Spectra of Pyridine Adsorbed at a Silver Electrode. *Chem. Phys. Lett.* **1974**, *26*, 163−166.

(6) Cardinal, M. F.; Vander Ende, E.; Hackler, R. A.; McAnally, M. O.; Stair, P. C.; Schatz, G. C.; Van Duyne, R. P. Expanding applications of SERS through versatile nanomaterials engineering. *Chem. Soc. Rev.* **2017**, *46*, 3886−3903.

(7) Nalbant Esenturk, E.; Hight Walker, A. R. Surface-enhanced Raman scattering spectroscopy via gold nanostars. *J. Raman Spectrosc.* **2009**, *40*, 86−91.

(8) Indrasekara, A. S. D. S.; Meyers, S.; Shubeita, S.; Feldman, L. C.; Gustafsson, T.; Fabris, L. Gold nanostar substrates for SERS-based chemical sensing in the femtomolar regime. *Nanoscale* **2014**, *6*, 8891−8899.

(9) Owens, F. Reproducible surface-enhanced Raman spectroscopy of small molecular anions. *Mol. Phys.* **2011**, *109*, 667−671.

(10) Yi, J.; You, E.-M.; Liu, G.-K.; Tian, Z.-Q. AI−nano-driven surface-enhanced Raman spectroscopy for marketable technologies. *Nat. Nanotechnol.* **2024**, *19*, 1758−1762.

(11) Masson, J.-F.; Biggins, J. S.; Ringe, E. Machine learning for nanoplasmonics. *Nat. Nanotechnol.* **2023**, *18*, 111−123.

(12) Quarin, S. M.; Vang, D.; Dima, R. I.; Stan, G.; Strobbia, P. AI in SERS sensing moving from discriminative to generative. *npj Biosensing* **2025**, *2*, 9.

(13) Vang, D.; Kelly, M. S.; Sheokand, M.; Sharma, M.; Esfandiari, L.; Dima, R. I.; Strobbia, P. Machine Learning Approaches in Label-Free Small Extracellular Vesicles Analysis with Surface-Enhanced Raman Scattering (SERS) for Cancer Diagnostics. *bioRxiv* **2024**.

(14) Lussier, F.; Thibault, V.; Charron, B.; Wallace, G. Q.; Masson, J.-F. Deep learning and artificial intelligence methods for Raman and surface-enhanced Raman scattering. *TrAC, Trends Anal. Chem.* **2020**, *124*, 115796.

(15) Thrift, W. J.; Ragan, R. Quantification of Analyte Concentration in the Single Molecule Regime Using Convolutional Neural Networks. *Anal. Chem.* **2019**, *91*, 13337−13342.

(16) Weng, S.; Yuan, H.; Zhang, X.; Li, P.; Zheng, L.; Zhao, J.; Huang, L. Deep learning networks for the recognition and quantitation of surface-enhanced Raman spectroscopy. *Analyst* **2020**, *145*, 4827−4835.

(17) He, J.; He, C.; Zheng, C.; Wang, Q.; Ye, J. Plasmonic nanoparticle simulations and inverse design using machine learning. *Nanoscale* **2019**, *11*, 17444−17459.

(18) Malkiel, I.; Mrejen, M.; Nagler, A.; Arieli, U.; Wolf, L.; Suchowski, H. Plasmonic nanostructure design and characterization via Deep Learning. *Light Sci. Appl.* **2018**, *7*, 60.
(19) Pan, Y.; Christiansen, R. E.; Michon, J.; Hu, J.; Johnson, S. G. Topology optimization of surface-enhanced Raman scattering substrates. *Appl. Phys. Lett.* **2021**, *119*, 061601.
(20) Vahidzadeh, E.; Shankar, K. Artificial Neural Network-Based Prediction of the Optical Properties of Spherical Core−Shell Plasmonic Metastructures. *Nanomaterials* **2021**, *11*, 633.
(21) Liu, Y.; Yin, S.; Liu, Z.; Zhang, H. A machine learning framework for process optimization in aerosol jet 3D printing. *Flex. Print. Electron.* **2023**, *8*, 025017.
(22) Wagner, M.; Distler, A.; Le Corre, V. M.; Zapf, S.; Baydar, B.; Schmidt, H.-D.; Heyder, M.; Forberich, K.; Lüer, L.; Brabec, C. J.; Egelhaaf, H.-J. Cutting "lab-to-fab" short: high throughput optimization and process assessment in roll-to-roll slot die coating of printed photovoltaics. *Energy Environ. Sci.* **2023**, *16*, 5454−5463.
(23) Queraltó, A.; Pacheco, A.; Jiménez, N.; Ricart, S.; Obradors, X.; Puig, T. Defining inkjet printing conditions of superconducting cuprate films through machine learning. *J. Mater. Chem. C* **2022**, *10*, 6885−6895.
(24) Brishty, F. P.; Urner, R.; Grau, G. Machine learning based data driven inkjet printed electronics: jetting prediction for novel inks. *Flex. Print. Electron.* **2022**, *7*, 015009.
(25) Shi, J.; Song, J.; Song, B.; Lu, W. F. Multi-Objective Optimization Design through Machine Learning for Drop-on-Demand Bioprinting. *Engineering* **2019**, *5*, 586−593.
(26) Carou-Senra, P.; Ong, J. J.; Castro, B. M.; Seoane-Viaño, I.; Rodríguez-Pombo, L.; Cabalar, P.; Alvarez-Lorenzo, C.; Basit, A. W.; Pérez, G.; Goyanes, A. Predicting pharmaceutical inkjet printing outcomes using machine learning. *Int. J. Pharm.:X* **2023**, *5*, 100181.
(27) Zhang, H.; Moon, S. K. Reviews on Machine Learning Approaches for Process Optimization in Noncontact Direct Ink Writing. *ACS Appl. Mater. Interfaces* **2021**, *13*, 53323−53345.
(28) Xu, W.; Liu, Z.; Piper, R. T.; Hsu, J. W. P. Bayesian Optimization of photonic curing process for flexible perovskite photovoltaic devices. *Sol. Energy Mater. Sol. Cells* **2023**, *249*, 112055.
(29) Zhang, J.; Liu, B.; Liu, Z.; Wu, J.; Arnold, S.; Shi, H.; Osterrieder, T.; Hauch, J. A.; Wu, Z.; Luo, J.; Wagner, J.; Berger, C. G.; Stubhan, T.; Schmitt, F.; Zhang, K.; Sytnyk, M.; Heumueller, T.; Sutter-Fella, C. M.; Peters, I. M.; Zhao, Y.; Brabec, C. J. Optimizing Perovskite Thin-Film Parameter Spaces with Machine Learning-Guided Robotic Platform for High-Performance Perovskite Solar Cells. *Adv. Energy Mater.* **2023**, *13*, 2302594.
(30) Pfeifer, S.; Pokuri, B. S. S.; Du, P.; Ganapathysubramanian, B. Process optimization for microstructure-dependent properties in thin film organic electronics. *Mater. Discovery* **2018**, *11*, 6−13.
(31) Shrivastava, A.; Kalaswad, M.; Custer, J. O.; Adams, D. P.; Najm, H. N. Bayesian optimization for stable properties amid processing fluctuations in sputter deposition. *J. Vac. Sci. Technol., A* **2024**, *42*, 033408.
(32) Nahvi, A.; Sadoughi, M. K.; Arabzadeh, A.; Sassani, A.; Hu, C.; Ceylan, H.; Kim, S. Multi-objective Bayesian optimization of super hydrophobic coatings on asphalt concrete surfaces. *J. Comput. Des. Eng.* **2019**, *6*, 693−704.
(33) Fales, A. M.; Yuan, H.; Vo-Dinh, T. Development of Hybrid Silver-Coated Gold Nanostars for Nonaggregated Surface-Enhanced Raman Scattering. *J. Phys. Chem. C* **2014**, *118*, 3708−3715.
(34) Turkevich, J.; Stevenson, P. C.; Hillier, J. A study of the nucleation and growth processes in the synthesis of colloidal gold. *Discuss. Faraday Soc.* **1951**, *11*, 55−75.
(35) Torres, J. A. G.; Lau, S. H.; Anchuri, P.; Stevens, J. M.; Tabora, J. E.; Li, J.; Borovika, A.; Adams, R. P.; Doyle, A. G. A Multi-Objective Active Learning Platform and Web App for Reaction Optimization. *J. Am. Chem. Soc.* **2022**, *144*, 19999−20007.
(36) EDBO+ Login. https://edboplus.org (accessed 05-23-2025).
(37) doyle-lab-ucla/edboplus. 2024. https://github.com/doyle-lab-ucla/edboplus (accessed 05-23-2025).
(38) Blank, J.; Deb, K. Pymoo Multi-Objective Optimization in Python. *IEEE Access* **2020**, *8*, 89497−89509.
(39) Shahriari, B.; Swersky, K.; Wang, Z.; Adams, R. P.; de Freitas, N. Taking the Human Out of the Loop: A Review of Bayesian Optimization. *Proc. IEEE* **2016**, *104*, 148−175.
(40) Ishizaka, A.; Nemery, P. *Multi-criteria Decision Analysis: Methods and Software*; John Wiley & Sons, 2013.
(41) Hassija, V.; Chamola, V.; Mahapatra, A.; Singal, A.; Goel, D.; Huang, K.; Scardapane, S.; Spinelli, I.; Mahmud, M.; Hussain, A. Interpreting Black-Box Models: A Review on Explainable Artificial Intelligence. *Cogn. Comput.* **2024**, *16*, 45−74.
(42) Le Ru, E. C.; Blackie, E.; Meyer, M.; Etchegoin, P. G. Surface Enhanced Raman Scattering Enhancement Factors: A Comprehensive Study. *J. Phys. Chem. C* **2007**, *111*, 13794−13803.
(43) Byram, C.; Moram, S. S. B.; Shaik, A. K.; Soma, V. R. Versatile gold based SERS substrates fabricated by ultrafast laser ablation for sensing picric acid and ammonium nitrate. *Chem. Phys. Lett.* **2017**, *685*, 103−107.
(44) Kumar, G.; Soni, R. K. Trace-Level Detection of Explosive Molecules with Triangular Silver Nanoplates-Based SERS Substrates. *Plasmonics* **2022**, *17*, 559−573.
(45) McDonnell, C.; Albarghouthi, F. M.; Selhorst, R.; Kelley-Loughnane, N.; Franklin, A. D.; Rao, R. Aerosol Jet Printed Surface-Enhanced Raman Substrates: Application for High-Sensitivity Detection of Perfluoroalkyl Substances. *ACS Omega* **2023**, *8*, 1597−1605.
(46) Liszewska, M.; Bartosewicz, B.; Budner, B.; Nasiłowska, B.; Szala, M.; Weyher, J. L.; Dzięcielewski, I.; Mierczyk, Z.; Jankiewicz, B. J. Evaluation of selected SERS substrates for trace detection of explosive materials using portable Raman systems. *Vib. Spectrosc.* **2019**, *100*, 79−85.

https://doi.org/10.1021/acsanm.5c01462
ACS Appl. Nano Mater. XXXX, XXX, XXX−XXX